J. Fluid Mech. (2021), *vol*. 913, A35, doi:10.1017/jfm.2020.1129

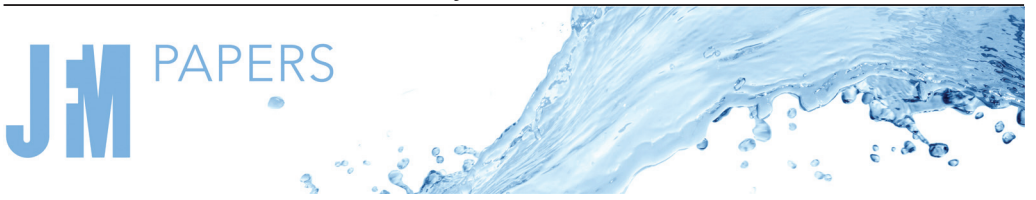

Spanwise velocity statistics in high-Reynolds-number turbulent boundary layers

R. Baidya[1],†, J. Philip[1], N. Hutchins[1], J.P. Monty[1] and I. Marusic[1]

[1]Department of Mechanical Engineering, The University of Melbourne, Victoria 3010, Australia

(Received 3 December 2019; revised 30 September 2020; accepted 14 December 2020)

Spanwise velocity statistics from high-Reynolds-number turbulent boundary layers are reported. The dataset combines efforts spanning over a decade at the University of Melbourne to accurately capture Reynolds number (Re) trends for the spanwise velocity, nominally over one order of magnitude change in Re, using custom subminiature cross-wire probes that minimise spatial resolution effects and misalignment errors. The spanwise velocity (v) variance is found to exhibit an Re invariant logarithmic slope in the log region, in a similar manner to the streamwise velocity (u), which is consistent with the existence of self-similar features within wall-bounded flows. However, unlike the u-variance, it appears that the logarithmic v-variance trend continues to extend towards the wall. The increase in the v-variance with Re in the log region is found to be due to 'intermediate-scale eddies', which follow distance-from-the-wall scaling. This results in the v-spectrogram exhibiting a dominant energetic ridge across the intermediate-scales, a trend that is not clearly observed in the u-spectrogram. Other features of the v-spectrogram are found to be similar to the u-spectrogram, such as showing small-scale near-wall features that scale universally with viscous units, and the influence of large-scale v signals residing in the log region that extend to the wall, resulting in a large-scale v footprint in the near-wall region. The observed behaviour of the v-spectrogram with changing Re is used to construct a model for the v-variance based on contributions from small-, intermediate- and large-scales, leading to a predictive tool at asymptotically high Re.

Key words: boundary layer structure, turbulent boundary layers

1. Introduction

Single-normal hot-wire anemometry has been successfully used to obtain sufficiently resolved streamwise velocity (u) data at moderate and high Reynolds numbers

† Email address for correspondence: baidyar@unimelb.edu.au

(Hultmark *et al.* 2012; Örlü & Schlatter 2013; Marusic *et al.* 2015; Samie *et al.* 2018). These studies and others show an increasing prominence of large-scale velocity fluctuations with Reynolds number (Re), such that, at sufficiently large Re, these contributions eventually become responsible for the majority of the turbulent kinetic energy production (Smits, McKeon & Marusic 2011). Furthermore, these large-scale u features are also known to alter the small-scale motions near the wall (Abe, Kawamura & Choi 2004; Hutchins & Marusic 2007*b*), resulting in amplitude modulation of the small-scales across all three velocity components (Talluru *et al.* 2014). Although the streamwise component of velocity has provided many valuable insights into the large-scale features residing in the log region, construction of a more comprehensive view of these features has been hindered by the scarcity of high-Re measurements surveying the spanwise (v) and wall-normal (w) velocity components. Here, we redress this issue through matched spatial resolution cross-wire measurements, where v or w (depending on the cross-wire probe orientation) is captured simultaneously with u. In addition to their scarcity, often inadequate attention has been given to the issue of spatial resolution when attempts have been made to measure the v and w fluctuations (e.g. Fernholz & Finley 1996). This can lead to misleading Re trends, due to a systematic variation in the spatial resolution introduced as a function of Re (e.g. when a free stream velocity is increased while a constant sensor size is maintained, see also Hutchins *et al.* (2009)). Accordingly, the present measurements are designed to capture cases where the spatial resolution is matched across a range of Re, allowing a cleaner extraction of any Re trends that may exist.

The challenges associated with measuring the spanwise or wall-normal velocity in wall-bounded flows are numerous. The reduced magnitude of v and w compared with u leads to a reduction in the signal-to-noise ratio. Near-wall measurements are further challenged by the increase in the physical sensor size that is typically required to measure the second velocity component. There are also challenges in accurately capturing the broad range of scales as Re increases, which for most facilities will result in a shrinking viscous length scale and demand ever-smaller sensor geometries. The work reported here represents a cumulation of effort undertaken at the University of Melbourne, spanning over a decade, which include: (i) building a large-scale wind tunnel facility, to effectively resolve small-scales even at a high-Re regime with conventional, well-established measurement techniques (Nickels *et al.* 2005; Marusic *et al.* 2015); (ii) an extensive investigation of finite dimension effects expected from a cross-wire probe of a certain physical size (Philip *et al.* 2013*a*,*b*; Baidya *et al.* 2019*b*); (iii) assessment of sensitivity to probe misalignment and calibration errors (Baidya *et al.* 2019*a*); (iv) development of a custom subminiature cross-wire probe designed to minimise the sources of errors found in the finite sensor dimension and probe misalignment investigations (Baidya 2016); and (v) development of a specialised calibration procedure (e.g. Morrill-Winter *et al.* 2015; Zimmerman, Morrill-Winter & Klewicki 2017).

Theoretical models that describe the scalings and Re trends for the second-order velocity statistics for wall turbulence are sparse, and those that have been developed, e.g. Monkewitz & Nagib (2015), have primarily focussed on the streamwise normal stress. Classical theory, that follows scalings based on the mean flow, such as law-of-the-wall and outer scalings (Millikan 1938), lead to the conclusion that all three components of inner-scaled velocity variance are constants across the log layer at asymptotically high Re (e.g. Perry & Abell 1975). Empirical data, however, show that this is not the case (Laufer 1954; Fernholz & Finley 1996; DeGraaff & Eaton 2000), leading Townsend (1976) to propose alternate scalings based on the attached eddy hypothesis (AEH). Townsend's (inviscid) theory considers a description of high-Re boundary layers to be composed of

self-similar attached coherent motions that scale with their distance from the wall, where the presence of the wall restricts the wall-normal velocity due to the impermeability condition, while the u and v fluctuations remain unrestricted. From this point of view, u and v are expected to show a similar behaviour, with their variances predicted to follow logarithmic profiles with wall-normal distance across the log layer. The AEH has become a prominent theory in the field (see the recent review by Marusic & Monty (2019)), and therefore, here, we compare our results with Townsend's predictions. Further, we examine and compare the related spectral energetic content of v against u and assess how the dominant scales are modified as a function of wall height and Re.

At low to moderate Re, direct numerical simulations (DNS) provide a more readily assessable avenue to examine the spanwise (and wall-normal) velocity compared with experiments. As an example, del Álamo *et al.* (2004) report that the energetic scales in v occur at a much finer streamwise wavelength compared with u. In addition, the spanwise velocity variance ($\overline{v^2}$) profiles demonstrate a clearer log–linear relation, consistent with Townsend's prediction, compared with the streamwise velocity intensities ($\overline{u^2}$), at least for the range of Re accessible through DNS (Sillero, Jiménez & Moser 2013; Mehrez *et al.* 2019).

Despite advances in understanding the physical mechanism governing wall-bounded turbulence permitted by DNS data, the asymptotic behaviour predicted by AEH may be masked in DNS data due to limited scale separation. For example, the slope of the log–linear behaviour is expected to be universal across wall-bounded flows (Marusic *et al.* 2013). However, for the DNS data, the slope of the logarithmic $\overline{v^2}$ behaviour in the external flows (boundary layer) is shallower compared with the internal flows (pipe and channel). Here, we use high-Re experimental data to assess if this logarithmic behaviour approaches a universal asymptomatic scaling.

As such, the purpose of the current paper is not only to present reliable spanwise velocity statistics using subminiature cross-wire probes, but also to highlight the unique characteristics of v pertaining to high-Reynolds-number turbulent boundary layers.

2. Experimental set-up

The current cross-wire measurements were conducted in the high-Reynolds-number boundary layer wind tunnel (HRNBLWT), located at the University of Melbourne. This facility is designed for studying high-Re turbulent boundary layers, while also ensuring relatively low free stream turbulence intensity levels where $\sqrt{\overline{u^2}}/U_\infty < 0.05 - 0.2\,\%$ depending on the streamwise location (Nickels *et al.* 2005; Marusic *et al.* 2015). The measurements are taken at three different x locations – 2, 7 and 18 m downstream of the tripped inlet to the working section. For the first set of measurements, the free stream velocity (U_∞) is fixed at 15 m s^{-1}, while the streamwise position is varied. Since the friction velocity is only weakly dependent on the streamwise distance (for a fixed free stream velocity), this allows measurements at different Re using the same probe while still ensuring that our viscous-scaled sensor size is relatively constant. In addition to the matched spatial resolution measurements, we extend the Re range by measuring at $U_\infty \approx 30$ m s^{-1} and $x \approx 18$ m using the same cross-wire probe. Consequently, the viscous length scales are now smaller and thus the spatial resolution is poorer relative to the 15 m s^{-1} cases. However, the large-scale contributions which are several orders of magnitude larger than the sensor size remain unaffected, and therefore the dataset provides useful Re trends for these scales.

Symbols	x (m)	U_∞ (ms^{-1})	Re_τ	ν/U_τ (μm)	U_τ (ms^{-1})	δ (m)	Δt^+	TU_∞/δ	l_x^+	l_y^+	$\Delta s_z^+, l_z^+$
●	2	14.7	2400	28	0.543	0.068	0.486	18 000	14	14	7 (Δs_z^+)
■	7	14.7	5000	30	0.508	0.151	0.422	19 000	13	13	7 (Δs_z^+)
♦	18	14.7	10 400	32	0.479	0.331	0.377	19 000	13	13	7 (Δs_z^+)
▲	18	29.8	18 400	17	0.925	0.310	0.688	20 000	24	24	12 (Δs_z^+)
☆	—	—	7.2×10^5	83	0.18	60	110	$O(100)$	600	600	1000 (l_z^+)

Table 1. Experimental parameters for the cross-wire measurements (solid symbols), configured to measure the streamwise and spanwise velocities. Also shown are the experimental parameters for the atmospheric surface-layer dataset (☆) from Hutchins *et al.* (2012). Here Δt and T denote the sampling interval and the total sampling time, respectively.

The details of the cross-wire experimental conditions (solid symbols) are summarised in table 1. Here, we employ the coordinate system x, y and z to refer to the streamwise, spanwise and wall-normal directions, respectively, and u, v and w the corresponding fluctuating velocities. The superscript '+' denotes viscous scaling of length (e.g. $z^+ = zU_\tau/\nu$), velocity (e.g. $U^+ = U/U_\tau$) and time (e.g. $t^+ = tU_\tau^2/\nu$), where U_τ and ν are the mean friction velocity and the kinematic viscosity of the fluid, respectively. Capitalisation (e.g. U) and overbar (e.g. $\overline{u^2}$) indicate time-averaged quantities. The symbols ●, ■ and ♦ in table 1 denote the cases where spatial resolution is maintained constant, while the highest Re case (▲) yields a relatively poorer spatial resolution. The value for friction velocity, U_τ, and boundary layer thickness, δ, given in table 1 have been obtained by fitting the mean velocity profile to a composite velocity formulation of Chauhan, Monkewitz & Nagib (2009). The sampling interval Δt is chosen so that it is sufficiently low, to capture the smallest energetic length scale (i.e. $\Delta t^+ < 3$, Hutchins *et al.* (2009)), while the total sampling time T corresponds to approximately 20 000 boundary layer turnover times (TU_∞/δ).

Figure 1 shows the custom cross-wire probe used, where dimensions occupied by 2.5 μm diameter platinum hot-wire sensors are 0.4×0.4 mm ($l_x \times l_y$) in the x and y directions with a separation of 0.2 mm (Δs_z) in the z direction. The hot-wire prongs are stainless steel wires of diameter 250 μm, ground down to a tip diameter of 20 μm, which are then inserted into specially designed ceramic holders. The prongs are copper plated before the platinum wires are soldered to them. An important feature of these prongs is that, although the whole probe body is tilted at approximately 10° towards the wall (to access near-wall velocity statistics), the hot-wires themselves are kept parallel to the wall. This feature, which unfortunately is not available in commercial probes, is essential in minimising errors arising from an inclination of the cross-wire sensor plane with respect to the wall. For example, Baidya *et al.* (2019*a*) showed that the inclined sensor plane cannot be fully accounted for through a typical calibration procedure, where contributions from the out-of-plane velocity are ignored. The inclined sensor plane results in increased sensitivity to the out-of-plane velocity component, leading to a large error of up to 10 % for the turbulent stresses in the log region. In addition, the custom probe allowed us to incorporate key design information provided from probe simulations into the design. That is, the custom probe is designed such that the wire separation distance is smaller than the wire length dimensions (see figure 1) since it is found that the former dominates the errors when measuring v (Philip *et al.* 2013*b*).

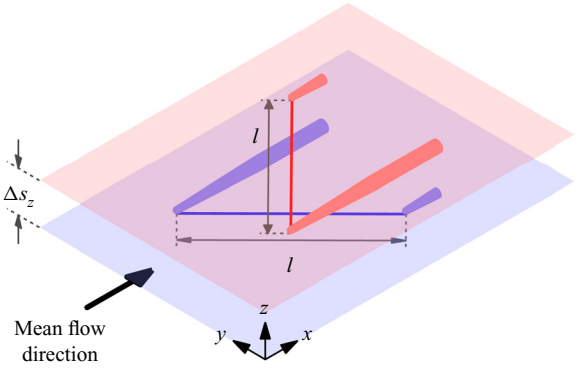

Figure 1. Schematic of a cross-wire probe configured to measure the streamwise and spanwise velocities. The red and blue wires are located on their respective coloured planes. l and Δs_z denote the sensor length and the spacing between the sensors (in the wall-normal direction), respectively.

The hot-wires are operated in constant temperature mode with an overheat ratio of 1.8, while a full two-dimensional calibration of the cross-wire probe is performed *in situ* using a calibration jet facility that rotates the jet about the wall-normal axis of the cross-wire sensors (for details, see Morrill-Winter *et al.* (2015)). During the two-dimensional calibration, the voltages from the two sensors are recorded at 12 to 17 different velocities across 0–1.1 U_∞ and 11 jet angles spanning $\pm 30^\circ$ about the z axis to build up a voltage-to-velocity conversion map. Figure 2(a) shows voltage pairs (E_1, E_2) obtained for multiple jet velocity and angle combinations during a typical two-dimensional calibration. In order to ensure a smooth voltage-to-velocity conversion map, the recorded voltages are fitted to a functional form. The functional form utilised for the current study prescribes (i) a collapse of hot-wire voltages curves as a function of effective velocity occurs across all jet angles (Browne, Antonia & Shah 1988) and (ii) the response of the hot-wire to the flow angles follows a sinusoidal function (Hinze 1975; Morrill-Winter *et al.* 2015). Third-order polynomials are used to describe the effective velocities as functions of the hot-wire voltages. Prescribing (i) and (ii), and assuming that the inclination angle of the two hot-wires are at $\pm 45^\circ$ with respect to the x direction (the cross-wire probes used in the experiments were designed such that the hot-wires are at $\pm 45^\circ$) results in

$$\left.\begin{aligned} \frac{U_{eff1}^2}{U_{jet}^2} &= \cos^2\left(\gamma + \frac{\pi}{4}\right) + k^2 \sin^2\left(\gamma + \frac{\pi}{4}\right) \\ &\text{and} \\ \frac{U_{eff2}^2}{U_{jet}^2} &= \cos^2\left(\gamma - \frac{\pi}{4}\right) + k^2 \sin^2\left(\gamma - \frac{\pi}{4}\right), \end{aligned}\right\} \tag{2.1a,b}$$

where U_{eff1} and U_{eff2} are effective velocities from the two hot-wires, U_{jet} and γ are, respectively, the jet velocity and angle with respect to the cross-wire probe and k is the axial sensitivity coefficient which usually varies from 0 to 0.2 (Champagne, Sleicher & Wehrmann 1967). Following algebraic and trigonometric manipulations (2.1) leads to $U_{eff1}^2 + U_{eff2}^2 = U_{jet}^2(1 + k^2)$, which corresponds to an equation for a circle. Figure 2(b) shows the effective velocities from the two-dimensional calibration shown in figure 2(a), where an equation for a circle provides a good description of the calibration points, particularly at higher jet velocities. Note that the effective velocities in figure 2(b) are

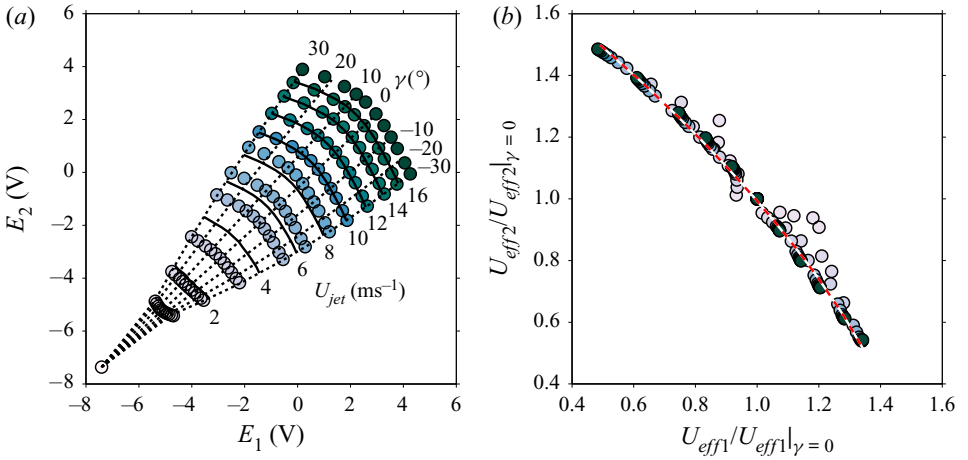

Figure 2. (*a*) Hotwire voltage (E_1, E_2) and (*b*) effective velocity (U_{eff1}, U_{eff2}) pairs from a typical two-dimensional cross-wire calibration. (*a*) Constant jet velocity (U_{jet}) and jet angle (γ) lines determined from calibration points are indicated as solid (—) and dotted (· · ·) lines. (*b*) The effective velocities at a constant jet velocity are shown normalised by the value at the zero jet angle, while a fitted circle is shown as a dashed line (- - -). The ○ symbols showing the calibration points in panels (*a*,*b*) are coloured according to the jet velocities.

shown normalised by the effective velocity at $\gamma = 0$, which is a constant factor of U_{jet} according to (2.1). At low velocities, the heat transferred from the hot-wire is no longer dominated by the forced convection (Collis & Williams 1959; Hatton, James & Swire 1970), presumably resulting in the departure from (2.1) observed in figure 2(*b*). In addition to the jet calibration, the calibration corresponding to zero jet angle is repeated in the wind tunnel. Thus, for a case when no misalignment exists between the calibration jet and the wind tunnel, the two calibration curves should be identical. However, in practice, a non-zero misalignment exists and the in-plane misalignment angle (the sensor plane is parallel to the x–y plane in the current study) can be determined such that the disparity between the hot-wire voltages at the zero jet angle after accounting for the misalignment and the wind tunnel calibration is minimised. It should be noted that, since the in-plane misalignment is the leading-order contributor to the error in the evaluated velocity (Baidya *et al.* 2019*a*), the influence of the out-of-plane misalignment is ignored for the current misalignment correction procedure. Here U and V are calculated from the corrected jet angle and jet velocity to create a voltage–velocity lookup table, and the recorded voltages during the course of profiling are linearly interpolated based on the lookup table to convert to velocities. In addition, the test-section temperature increased more severely for the 30 m s^{-1} dataset compared with the 15 m s^{-1} cases. This meant that the difference in the ambient temperature during the two-dimensional calibration and the experiment was more pronounced for the 30 m s^{-1} dataset. Hence, the hot-wire voltages for the 30 m s^{-1} experiments were offset by values $(\Delta E_1, \Delta E_2)$ such that the compensated U profile agreed with the single-normal hot-wire measurements. Note that the offset voltages ΔE_1 and ΔE_2 are functions of z, and correspond to the change in the hot-wire voltages due to different ambient conditions.

The final dataset considered are measurements from the atmospheric surface layer, obtained utilising three-component sonic anemometers (Campbell Scientific CSAT3), from Hutchins *et al.* (2012). The surface layer experiments allow access to very high Re, which is difficult to achieve in the laboratory, allowing the assessment of Re trends to be

extended to $Re_\tau \equiv U_\tau \delta/\nu \sim O(10^6)$. The dataset presented here (denoted using symbol ☆) corresponds to an hour of measurement, carefully selected from nine days of available measurements based on the requirement of near-neutral stability, appropriate incoming flow direction relative to the sonic anemometer and steady wind (see Hutchins *et al.* (2012), for full details of data selection criteria). Velocity measurements from nine sonic anemometers logarithmically spaced from $z = 1.42$ m to 25.69 m on a vertical tower are considered here. The corresponding friction-based Reynolds number is estimated to be $Re_\tau \approx 7.2 \times 10^5$, where U_τ is calculated under the assumption that the viscous scaled Reynolds shear stress peaks at unity, while δ is inferred based on turbulent stress profiles and two-point correlations.

3. Moments of the spanwise velocity

Figures 3(*a*) and 3(*b*) show the second moment (variance) of the spanwise velocity, $\overline{v^2}$, where the wall distance is normalised with viscous and outer units, respectively. The vertical error bars denote uncertainty levels in $\overline{v^2}$, estimated as $\pm 5\,\%$ for the lower Re laboratory data ($Re_\tau \approx 2500$–$10\,000$) and $\pm 10\,\%$ for the $Re_\tau \approx 18\,000$ dataset. These error bars are estimated based on cross-wire probe uncertainty analysis (Baidya *et al.* 2019*a*), uncertainty in determining the friction velocity (Winter 1979; Klewicki *et al.* 2007) and the spread in statistics observed during experiment repeats. The peak $\overline{v^2}^+$ occurs at $z^+ \approx 50$, which is farther away from the wall than the $\overline{u^2}^+$ peak location at $z^+ \approx 15$ (Sillero *et al.* 2013; Lee & Moser 2015). In the log region (i.e. where the mean velocity is seen to follow a log law – shown by horizontal bars in figure 3*a*), $\overline{v^2}$ follows a log–linear relationship in a similar manner to the $\overline{u^2}$ statistics, given by,

$$\frac{\overline{v^2}}{U_\tau^2} = -A_2 \ln \frac{z}{\delta} + B_2, \tag{3.1}$$

where A_2 and B_2 indicate the logarithmic slope and intercept of the fit, respectively. The slope of the logarithmic behaviour in figure 3 is consistent across the dataset with a matched spatial resolution (●, ■, ♦) and with the $\overline{v^2}$ statistics from DNS (dotted and dash-dotted lines), while a shallower slope is recorded for the $Re_\tau \approx 18\,000$ dataset. This is because a lower spatial resolution sensor leads to underestimated smaller scales, causing $\overline{v^2}$ statistics to be increasingly attenuated closer to the wall (Philip *et al.* 2013*b*). For the current experiment, the $\overline{v^2}$ errors due to the finite sensor effects become prominent below $z^+ \lesssim 100$ (indicated by a vertical dash-dotted line in figure 3*a*) where the biases introduced exceed the uncertainty of the experiment (which is equal to ± 5 and $\pm 10\,\%$ for the $U_\infty = 15$ and 30 m s^{-1} cases, respectively). The slope of the logarithmic $\overline{v^2}$ behaviour for the $Re_\tau \approx 10\,000$ dataset, based on a linear regression in the region $3\sqrt{\delta^+} \leqslant z^+ \leqslant 0.15\delta^+$ (indicated by the green horizontal bar in figure 3*a*), provides $A_2 \approx 0.27$. It should be noted that the lower bound selected for the log region is based on a z location where the inertial forces become leading order in the mean momentum balance (Morrill-Winter, Philip & Klewicki 2017), which also coincides with an onset of a logarithmic behaviour in both the U and $\overline{u^2}$ statistics (Marusic *et al.* 2013). Furthermore, setting $A_2 = 0.27$, the value for B_2 based on the regression varies from 1.3 at $Re_\tau \approx 2500$ to 1.5 at $Re_\tau \approx 10\,000$ (only the matched spatial resolution cases are considered to isolate the Re effects) as shown in figure 4. The A_2 and B_2 values from the current study are in good agreement with

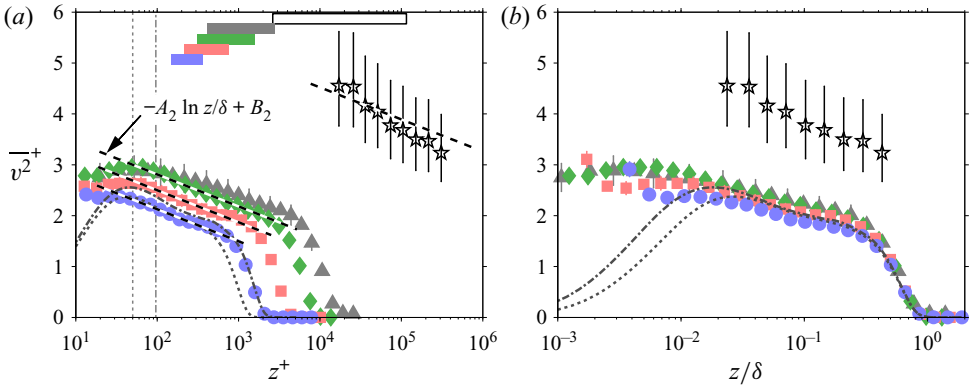

Figure 3. Variance of the spanwise velocity, $\overline{v^2}$, shown in (*a*) viscous and (*b*) outer normalisations. The solid symbols (●, ■, ♦, ▲) correspond to measurements conducted at HRNBLWT, while the empty symbol (☆) is an atmospheric surface layer dataset obtained using a sonic anemometer, from Hutchins *et al.* (2012). The dotted and dash-dotted lines are $\overline{v^2}$ statistics from the DNS database of Schlatter & Örlü (2010) and Sillero *et al.* (2013), respectively. (*a*) The vertical dotted and dash-dotted line correspond to $z^+ = 50$ and $z^+ \approx 100$, respectively, while the dashed lines show log–linear relations with the slope $A_2 = 0.27$. Furthermore, the horizontal bars, coloured according to the corresponding *Re*, denote the location of the log region ($3\sqrt{\delta^+} \leqslant z^+ \leqslant 0.15\delta^+$).

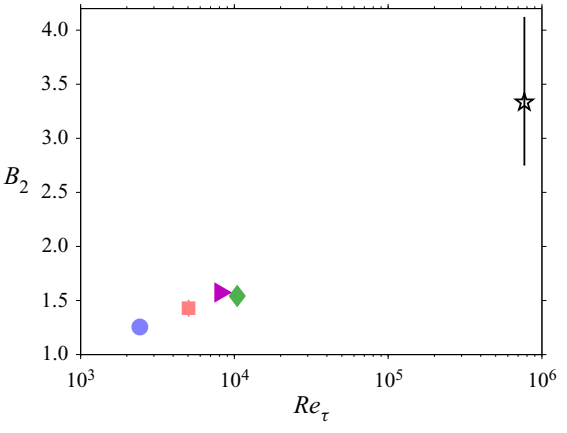

Figure 4. The logarithmic intercept, B_2, for the $\overline{v^2}$ statistics as a function of Re_τ. The magenta symbol, ▶, corresponds to measurements by Zimmerman *et al.* (2019) (where the B_2 value has been recomputed utilising a consistent definition for the log region and δ as the current study).

Zimmerman *et al.* (2019), who obtained $A_2 \approx 0.26$ and $B_2 \approx 1.6$ at $Re_\tau \approx 8000$ in the same facility (the HRNBLWT) with a different probe. Here, the A_2 and B_2 values for the Zimmerman *et al.* (2019) data have been re-evaluated, based on the definition for the log region and δ that is consistent with the current study. Hence, the value of B_2 differs slightly from that given in Zimmerman *et al.* (2019), where the boundary layer thickness is taken to be the z location where $U = 0.99U_\infty$. Note that, Zimmerman *et al.* (2019) obtain a somewhat different value of $A_2 \approx 0.34$, when they measure in the Flow Physics Facility. However, this difference is presumed to be due to an underdeveloped wake found in the Flow Physics Facility, where the velocity profile beyond $z/\delta \geqslant 0.8$ is found to deviate from the canonical profile (Zimmerman *et al.* 2019).

Also shown in figure 3 are the $\overline{v^2}$ statistics measured in the atmospheric surface layer by Hutchins *et al.* (2012), and denoted by ☆. These field measurements have larger uncertainties (the error bars reflect $\pm 10\,\%$ uncertainty in the friction velocity due to the assumption that $-\overline{uw}^+$ peaks at unity) compared with the laboratory measurements. Although the large uncertainty means that a wide range of A_2 is permissible to describe the log–linear $\overline{v^2}$ behaviour, $A_2 = 0.27$ is nevertheless consistent with the measurements (see dashed lines, figure 3*a*).

In the context of AEH, an increase in Re is reflected by a larger number of self-similar hierarchy levels required to model the wall-bounded flow. Thus, since the u and v contributions from each hierarchy level are additive, $\overline{u^2}^+$ and $\overline{v^2}^+$ at a fixed z^+ increases proportionally with the number of hierarchy levels, which scales as $\log \delta^+$ (Perry & Chong 1982). Indeed, an increase in $\overline{v^2}^+$ at a fixed z^+ location is observed in the current experiments (see figure 3*a*). Notably, the slope of logarithmic $\overline{v^2}$ ($A_2 \approx 0.27$) is shallower than that found in $\overline{u^2}$, where $A_1 \approx 1.2$ (Marusic *et al.* 2013). If one accepts the AEH description, a possible explanation for the difference in the slope between the $\overline{u^2}$ and $\overline{v^2}$ behaviour is that the wall-bounded flow is better represented by a hierarchy of multiple streamwise aligned eddies travelling in a packet (Adrian, Meinhart & Tomkins 2000), rather than a hierarchy of single isolated eddies where the logarithmic slopes observed for $\overline{u^2}$ and $\overline{v^2}$ are similar (i.e. $A_1 \approx A_2$). The streamwise aligned eddies lead to a strengthening of the u contributions per hierarchy level, while the v contributions remain relatively unaffected, leading to $A_1 > A_2$, which is more consistent with the experimental data (Baidya *et al.* 2014).

In the asymptotic limit, AEH predicts that B_2 will reach a constant, in a similar manner to the $\overline{u^2}$ behaviour, where the logarithmic intercept, B_1, also approaches a constant. While the empirical evidence supports B_1 approaching a constant at sufficiently high Re (Marusic, Uddin & Perry 1997; Marusic *et al.* 2013), an increase in B_2 is observed for the current dataset with increasing Re, as shown in figure 4 on log–linear axes. Furthermore, the atmospheric surface layer measurement suggests that B_2 might maintain a $\log \delta^+$ behaviour despite an increase in Re by over an order of magnitude. We note that, it is difficult to draw a robust conclusion on Re-dependency of B_2 based on figure 4 and further high quality $\overline{v^2}$ measurements in the $Re_\tau \sim 10^4$–10^6 range are necessary to make a more definitive conclusion. A discrepancy between the AEH predictions and the experimental results is also observed in terms of the spanwise velocity tendency to exhibit extreme values compared with a Gaussian distribution. That is, the v flatness values exceed 3 (super-Gaussian behaviour) in the log region (e.g. Fernholz & Finley (1996), and this is consistent with our observations too, but not shown here for brevity) while a value lower than 3 (sub-Gaussian behaviour) is predicted by AEH (Woodcock & Marusic 2015). This is in contrast to the u signal, which exhibits sub-Gaussian behaviour as predicted by AEH. Consequently, the higher-order even moments of u and v also behave differently – e.g. the logarithmic slope for the higher-order moments increasingly deviate away from a Gaussian behaviour in the opposite direction (Meneveau & Marusic 2013; Yang *et al.* 2018). The discrepancy between the experiment and AEH predictions is thought to arise due to a degree of correlation being retained among eddies of different scales in a real flow (Meneveau & Marusic 2013). For example, de Silva *et al.* (2016) showed that an introduction of a slight non-randomness in AEH hierarchy, whereby a restriction is imposed on the placement of eddies such that a minimum separation is maintained (i.e. two eddies from the same hierarchy level cannot coexist at the same location), results in a u and v behaviour that is more consistent with the experiments.

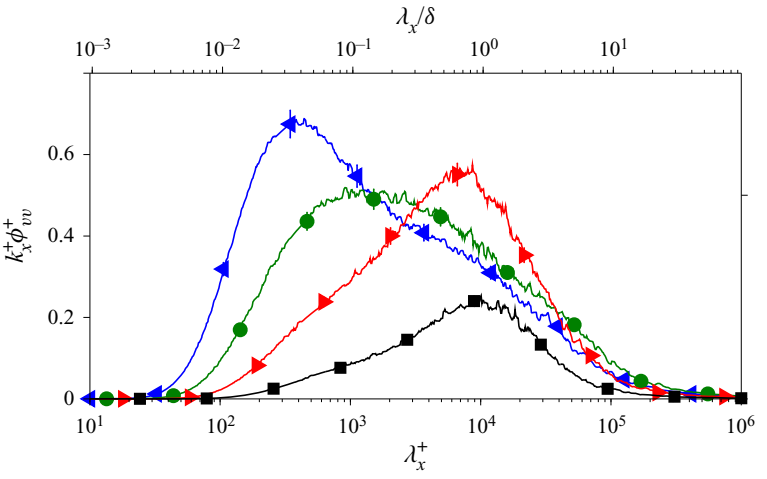

Figure 5. Premultiplied energy spectra of v fluctuations for a $Re_\tau \approx 10\,000$ turbulent boundary layer. The v spectra shown correspond to the wall heights $z^+ = 50$ (◀), $z^+ = 3\sqrt{\delta^+}$ (●), $z = 0.15\delta$ (▶) and $z = 0.6\delta$ (■), as indicated in figure 6(*c*).

4. Energy spectral density

Figure 5 shows the energy spectral density of v as a function of streamwise wavelength, λ_x, at selected z locations for the $Re_\tau \approx 10\,000$ case. The premultiplied energy spectra of spanwise velocity fluctuations, $k_x\phi_{vv}$, provide a measure of $\overline{v^2}$ contributions for a given streamwise length scale, since $\int_0^\infty k_x\phi_{vv}\,\mathrm{d}\ln k_x = \overline{v^2}$, where k_x corresponds to the streamwise wavenumber (i.e. $\lambda_x = 2\pi/k_x$). Note that, the energy spectral density, ϕ_{vv}, is a function of k_x (or λ_x) and therefore is distinct from (but related to) the spectral density per unit non-dimensional wavenumber $k_x\mathcal{L}$, $\Phi_{vv}(k_x\mathcal{L})$, where $\mathcal{L}$ is some length scale of interest (for further details see Nickels & Marusic (2001)), used by Perry & Chong (1982) and in the subsequent works.

It is evident from figure 5 that within the log region the most energetic wavelength becomes longer with wall distance (e.g. ● and ▶), while in the outer layer it remains relatively fixed at $\lambda_x \approx \delta$ (e.g. ▶ and ■). It should be noted that the temporal hot-wire signals have been converted to the spatial domain by invoking Taylor's frozen turbulence hypothesis (Taylor 1938), where the turbulent motions at all length scales are assumed to convect at the local mean velocity, $U(z)$. However, it is known that the convection velocity is scale-dependent (del Álamo & Jiménez 2009; Monty & Chong 2009); hence, we expect a slight change in the actual shape of the v spectrum following this procedure. Although we cannot entirely rule out its influence here, we expect the redistribution of energy beyond the log region ($z^+ \geqslant 3\sqrt{\delta^+}$, see vertical dashed lines in figure 6) to correspond to a small fraction of the overall energy, as at these z locations the convection velocity across the scales become more uniform (del Álamo & Jiménez 2009).

Figure 6(*a–c*) display the full map of the v-spectrogram at various Re, where the colours indicate the energetic content at a particular wall height and wavelength. Hence, the v spectra shown in figure 5 correspond to $k_x\phi_{vv}$ along the vertical lines in figure 6(*c*) with a matched symbol. Unlike the u-spectrogram (e.g. Hutchins & Marusic (2007*a*) and also figure 12(*a*) in appendix A) there is no apparent inner/outer site separation even at the highest Re data. Rather, it appears that for $z^+ < 70$, there exists a ridge of energy at a fixed streamwise wavelength $\lambda_x^+ \approx 350$. Through the log region, there are clear signs of

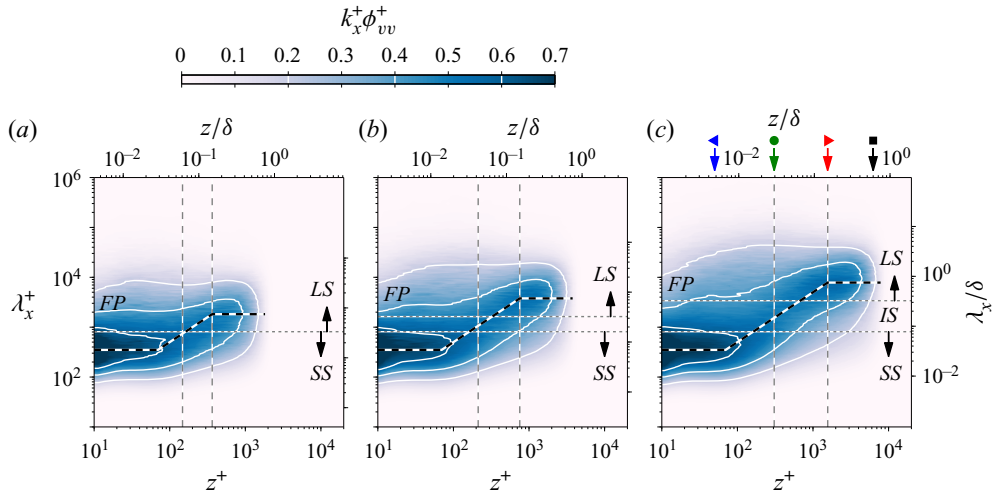

Figure 6. Premultiplied energy spectrogram of v fluctuations as a function of wall height, z, and wavelength, λ_x, at (*a*) $Re_\tau \approx 2500$, (*b*) $Re_\tau \approx 5000$ and (*c*) $Re_\tau \approx 10\,000$. The vertical dashed lines indicate the bounds of the log region, which are taken here to be $z^+ = 3\sqrt{\delta^+}$ and $z/\delta = 0.15$, while the black dashed lines show the location of the energetic ridge identified. The solid white lines correspond to contour levels 0.2, 0.4 and 0.6. Here '*FP*' denotes the location of the energetic 'footprint' from the very large-scale structure. The wavelengths corresponding to small-, intermediate- and large-scales are denoted by *SS*, *IS* and *LS*, respectively.

energy scaling with distance from the wall, with the energetic ridge seeming to follow the line $\lambda_x = 5z$ for $70 \leqslant z^+ \leqslant 0.15\delta^+$. Moreover, in the wake region, the energy seems to reach a ridge at a constant $\lambda_x/\delta \approx 0.75$. The energetic ridge, adhering to these trends, is indicated by the black dashed lines in figure 6. The distribution of the energetic u content relative to the location of the black dashed line in figure 12(*a*) of appendix A, indicates that the u fluctuations are dominated by energetic scales that are at a longer streamwise wavelength than the v fluctuations. This is due to the tendency of u fluctuations to align in the streamwise direction, while the spanwise velocity regions remain isolated (Sillero, Jiménez & Moser 2014).

Figure 6(*a–c*) also indicate that the small-scale, near-wall v spectral content is invariant with Reynolds number when scaled in viscous units. Note that, although the effects from finite sensor dimensions (the v spectra closely follow the w spectra behaviour described in Baidya *et al.* (2019*b*)) become more severe in the near-wall region, we expect this effect to remain constant across figure 6(*a–c*) since we have maintained a matched spatial resolution (Philip *et al.* 2013*b*; Baidya *et al.* 2019*b*). Similarly, even though the assumption that the convection velocity for Taylor's hypothesis is equal to the local mean velocity is less valid in the near-wall region (del Álamo & Jiménez 2009), the redistribution of the energetic content in the v-spectrogram is expected to be similar across the three *Re* cases. In contrast to the invariance of the near-wall v-spectrogram when $\lambda_x^+ \lesssim 1000$, the contours outside this region shift towards higher λ_x^+ with increasing *Re*. This is likely because, in a similar manner to the streamwise velocity (e.g. Hutchins & Marusic (2007*a*), and also figure 12(*a*), in appendix A) the influence of the very large-scale features that reside in the log region extends to the wall for the spanwise velocity. Thus, the very large-scale feature has a footprint that extends to the wall, leading to large-scale energetic content in v at $z^+ \sim 10$ and $\lambda/\delta \sim 1$ (this location is indicated by '*FP*') as shown in figure 6. Note that, although the presence of the large-scale footprint at the wall leads

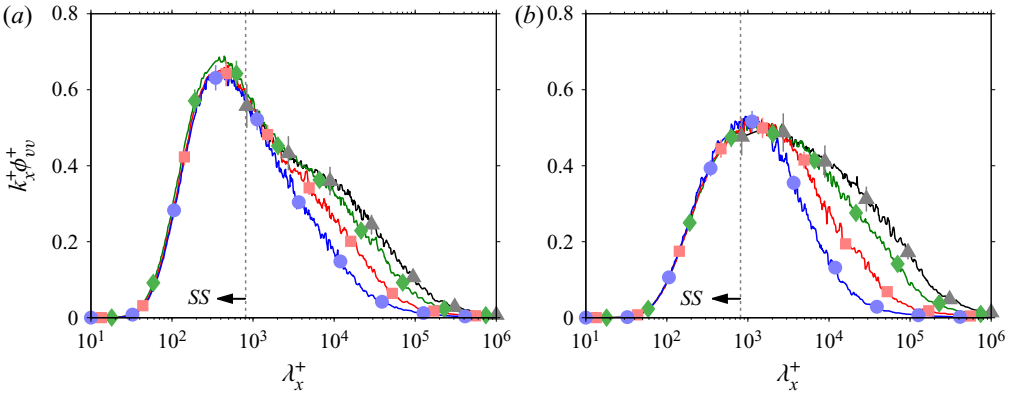

Figure 7. Premultiplied v spectra at (*a*) near-wall ($z^+ = 50$) and (*b*) log ($z^+ = 310$) regions. The symbols •, ■, ♦, ▲ correspond to $Re_\tau \approx 2500$, 5000, 10 000 and 18 000 cases, respectively.

to small-scales that are more strongly modulated with the large-scale u at high Re (Mathis, Hutchins & Marusic 2009; Talluru *et al.* 2014), the small-scale energetic content seems to be preserved on the time-averaged sense, and therefore exhibits Reynolds number invariance when scaled in viscous units. Notably, the energetic footprint is absent from the w-spectrogram and the Reynolds shear stress cospectrogram (as shown by Baidya *et al.* (2017), and reproduced in figure 12*b*,*c*), due to the impermeability condition at the wall, which restricts large-scale wall-normal fluctuations in this region (Perry & Chong 1982). Furthermore, in an analogous manner to the classical mean flow theory (e.g. Millikan 1938), the peak contribution in the v-spectrogram and the uw-cospectrogram (and to a lesser extent w-spectrogram) follow a viscous and δ scaling in the near-wall and outer part of the boundary layer, respectively, while a transition from these two regimes occurs in the log region where the dominant modes scale with z.

Figure 7(*a*,*b*) show the influence of the Reynolds number on the v energetic content at the near-wall ($z^+ = 50$) and log ($z^+ = 3\sqrt{\delta^+} \approx 310$ at $Re_\tau \approx 10\,000$) regions, respectively. Here, the vertical dotted line indicates the spectral cutoff limit for the small-scale contribution (the choice for the cutoff wavelength is detailed in § 4.1). The small-scale spectral-cutoff also corresponds to the lower horizontal dotted lines in figure 6(*a–c*). Thus, the intermediate- and large-scale v fluctuations, where λ_x exceeds the cutoff value (the intermediate- and large-scales are distinguished in § 4.1), are responsible for an increase in the peak $\overline{v^2}$ observed at $z^+ = 50$ as a function of Re. Note that, due to poorer spatial resolution, the small-scale energetic content is not as well-resolved for the $Re_\tau \approx 18\,000$ dataset as the other three cases, and therefore this part of the spectrum is not shown in figure 7. The increase in the combined contribution from the intermediate- and large-scales to the broadband $\overline{v^2}$ observed in the near-wall region at high Re may provide clues on the scalability of the flow control strategies, which introduce oscillation or travelling waves at the wall to alter the near-wall v (Choi, Moin & Kim 1994; Quadrio 2011). These strategies achieve drag reduction by suppressing the near-wall streaks (Karniadakis & Choi 2003; Quadrio 2011), which are increasingly modified by the intermediate- and large-scale contributions at high Re (Hutchins & Marusic 2007*b*; Talluru *et al.* 2014); providing an additional mechanism that may explain the reduced drag performance observed with increasing Re (Hurst, Yang & Chung 2014; Gatti & Quadrio 2016).

In AEH, the logarithmic behaviour of $\overline{v^2}$ is associated with a $\phi_{vv} \sim k_x^{-1}$ behaviour (as with u) when a sufficient scale separation exists between the viscous and inertial scales (Perry, Henbest & Chong 1986). However, no distinct plateau region, spanning across an increasingly wide range of scales at higher Re (as envisioned by Perry *et al.* 1986) exists in figure 7(*b*). Hence, even though ϕ_{vv} shows clear signs of energy scaling with z in the log region, there is no evidence of $\phi_{vv} \sim k_x^{-1}$ behaviour for our experiment. Instead, a peak in energetic contribution occurs at $\lambda_x^+ \approx 1100$ and a shallower departure from the maxima occurs at higher Re for $\lambda_x^+ \gtrsim 1100$ (contributions below $\lambda_x^+ \lesssim 1100$ are Reynolds number invariant). Thus, the slope of the departure may eventually approach zero at sufficiently high Re ($Re_\tau \gg O(10^4)$), transforming the peak into a plateau. Note that, a self-similar hierarchy of eddies do not necessarily guarantee a k_x^{-1} behaviour, such as for a case when insufficient scale separation exists between the smallest and largest hierarchy levels (Davidson, Nickels & Krogstad 2006; Baidya *et al.* 2017). Nevertheless, the Re trend observed in figure 7(*b*) is consistent with the AEH calculations for these limited scale separation cases, where an increasingly plateau-like behaviour occurs when the scale separation is increased.

4.1. *Scale-decomposed $\overline{v^2}$ contributions*

To further quantify how the v-spectrogram behaviour changes with Re, we will divide the $k_x\phi_{vv}$ contribution into the small, intermediate and large wavelengths, using cutoff values (denoted by the horizontal lines) as illustrated in figure 6. Since small-scale energy scales with viscous units, the limit λ_{c1} is set in this inner-normalisation. Meanwhile, the large-scale energy scales with the outer scale, and therefore λ_{c2} is set to be a constant fraction of δ. This grouping implies that the separating thresholds (λ_{c1} and λ_{c2}) will move apart as Re (i.e. scale separation) increases. Therefore, the range of scales that will be grouped within the 'intermediate' range grows with Re.

The three regions in the v-spectrogram are integrated with respect to λ_x, and hence $\overline{v^2}$ can be decomposed based on the small- ($\overline{v^2}_{SS}$), intermediate- ($\overline{v^2}_{IS}$) and large-scale ($\overline{v^2}_{LS}$) contribution. That is,

$$\begin{aligned}\overline{v^2} &= \int_0^{\lambda_{c1}} k_x\phi_{vv}\,\mathrm{d}\ln\lambda_x + \int_{\lambda_{c1}}^{\lambda_{c2}} k_x\phi_{vv}\,\mathrm{d}\ln\lambda_x + \int_{\lambda_{c2}}^{\infty} k_x\phi_{vv}\,\mathrm{d}\ln\lambda_x \\ &= \overline{v^2}_{SS} + \overline{v^2}_{IS} + \overline{v^2}_{LS}. \end{aligned} \tag{4.1}$$

In the v-spectrogram, the energetic ridge at $\lambda_x^+ \approx 350$ and $\lambda_x \approx 0.75\delta$ across a range of z locations suggest that they result from viscous and δ-scaled structures, respectively. Thus, to demarcate the small- and large-scale contributions, the geometric centre between these two streamwise wavelengths is selected at the lowest Re ($Re_\tau \approx 2500$); therefore,

$$\lambda_{c1}^+ = \sqrt{350 \times 1875} = 810. \tag{4.2a}$$

Furthermore, λ_{c2} is chosen so that $\lambda_{c2} = \lambda_{c1}$ at $Re_\tau \approx 2500$, i.e.

$$\lambda_{c2} = 0.32\delta. \tag{4.2b}$$

Hence, the contributions from the intermediate-scales $\overline{v^2}_{IS}$ is equal to zero for the lowest Re case. It should be noted that, since the turbulence is broadband, no clear boundary exists between the small-, intermediate- and large-scale contributions. Therefore, equally valid choices for the integral limits used in (4.1) could exist, different from the current definition.

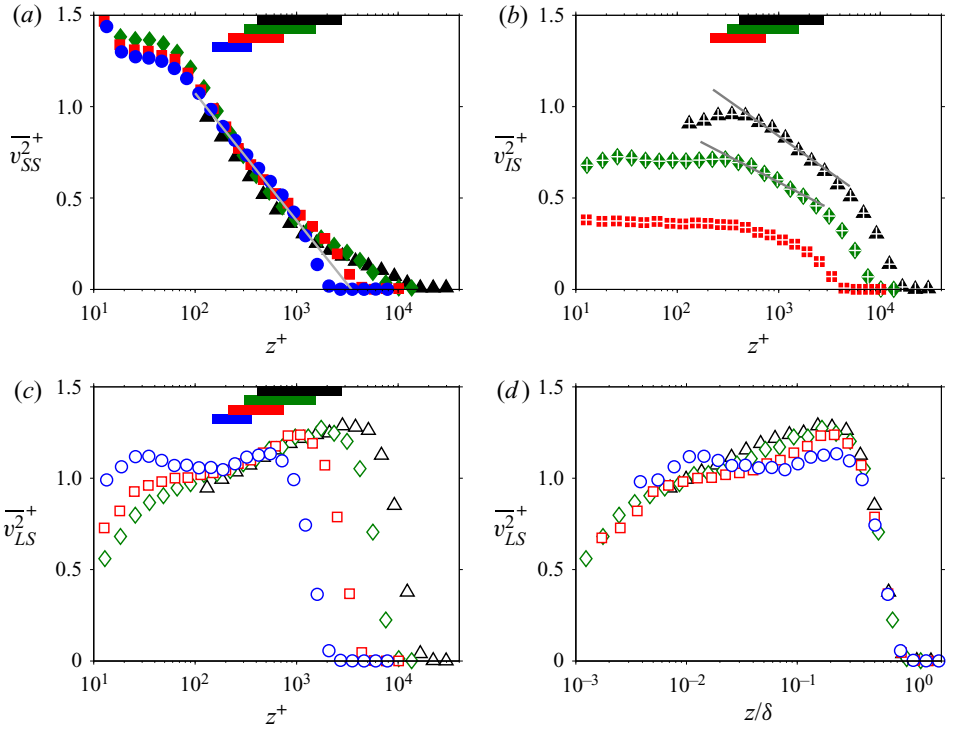

Figure 8. Scale-decomposed $\overline{v^2}$. (*a–c*) Small-, intermediate- and large-scale contributions as functions of z^+. (*d*) Large-scale contributions shown against z/δ. The symbols denote different *Re*: ○, $Re_\tau \approx 2500$; □, $Re_\tau \approx 5000$; ◇, $Re_\tau \approx 10\,000$; △, $Re_\tau \approx 18\,000$. The solid, chequered and open symbols correspond to the small-, intermediate- and large-scale contributions. The horizontal bars in panels (*a–c*) show the location of the log region and are coloured according to the corresponding *Re*, while the solid lines demonstrate log–linear relations.

Note that, altering the integral limits would change the $\overline{v^2}$ contributions associated with each scale; however, the focus here is on the *Re* trends, which remain relatively unaffected (provided that the viscous and δ scaling is used, respectively, for the integral limits λ_{c1} and λ_{c2}).

Figure 8(*a*) shows that $\overline{v^2}^+_{SS}$ is invariant in the near-wall region when the spatial resolution is comparable, similar to the $\overline{u^2}$ statistics (e.g. Hutchins *et al.* (2009), and also figure 13(*a*) in appendix A). Furthermore, the small-scale invariance is found to be universal across all turbulent stresses, when the procedure is repeated for the other velocity components (see appendix A for further details). Hence, these *Re* invariant contributions are likely to be associated with the buffer layer streaks (Kim, Kline & Reynolds 1971) and the quasi-streamwise vortices (Jeong *et al.* 1997), where the dominating contribution scales with viscous units (Jiménez & Moin 1991).

As expected, a strengthening of the intermediate-scale contribution occurs in figure 8(*b*) as *Re* increases, since the hierarchy of eddies contributing to $\overline{v^2}_{IS}$ extends with increasing *Re*. Note that the contribution at $Re_\tau \approx 2500$ to intermediate-scale is equal to zero based on (4.2). The importance of intermediate-scales becomes clear if we consider the high-*Re* limit, where evidence suggests that the hierarchy of eddies that are sufficiently separated from the viscous and inertially dominated scales exhibit self-similarity (Hwang & Sung

2018; Marusic & Monty 2019). Furthermore, with increasing Re, data in figure 8(b) show logarithmic behaviour within the inertial regime, which are made evident by the grey solid lines. This feature of the intermediate-scale would be employed later in § 4.2 (and figure 11) to construct a model for $\overline{v^2}$ in the high-Re limit.

Figure 8(d) shows the large-scale contributions to $\overline{v^2}$ in outer scaling. A good collapse of $\overline{v^2}^+_{LS}$ is observed for $z/\delta > 0.5$, with a peak contribution at $z/\delta \approx 0.2$. Notably, a simple decomposition based on a spectral cutoff is more successful in demarcating the viscous and δ-scaled contributions for v compared with u. This is because the viscous and δ-scaled energetic contributions are confined to a narrow wavelength band around the energetic ridge for v fluctuations, whereas for the u-spectrogram the energetic contributions about the local peaks occur over a wider wavelength band (compare figures 6c and 12a). It should be noted that for the $Re \approx 2500$ case, a secondary peak exists in the near-wall region ($z^+ < 100$) for $\overline{v^2}_{LS}$ due to inadequate scale separation, while it is absent in the higher Re cases. Thus, for the subsequent analysis this near-wall region below $z^+ < 100$ is ignored. Figure 9 shows a comparison of how the maxima in $\overline{v^2}_{LS}$ above $z^+ > 100$ varies with Re. Furthermore, the same procedure is applied for other turbulent stresses, where the symbols ▼, ■ and • show the maxima in $\overline{u^2}_{LS}$, $\overline{w^2}_{LS}$ and $-\overline{uw}_{LS}$, respectively. Note that, to account for energetic contribution at larger λ_x, the streamwise cutoff wavelengths $\lambda^+_{c1} = 2500$ and $\lambda_{c2}/\delta = 1$ are used for the streamwise velocity, while the limits given in (4.2) are maintained for demarcating the $\overline{w^2}$ and $-\overline{uw}$ stresses (see appendix A for further details). At low Re ($Re_\tau \approx 2500$–5000) an increase in the peak $\overline{v^2}^+_{LS}$ contribution is observed with increasing Re in a similar manner to the peak $\overline{u^2}^+_{LS}$ behaviour; however, the observed growth rate compared with $\overline{u^2}^+_{LS}$ is smaller. At increased Re, the data show that the maximum values deviate from the $\log \delta^+$ behaviour observed at low Re, and the growth as a function of Re is reduced. Therefore, at sufficiently high Re, the peak $\overline{u^2}^+_{LS}$ and $\overline{v^2}^+_{LS}$ may asymptote to constants. However, these highest Reynolds number data are the most experimentally challenging to obtain, and repeated measurements at even higher Re data are required to confirm these trends. The data also suggest that the peak $\overline{w^2}^+_{LS}$ and $-\overline{uw}^+_{LS}$ exhibit Re invariance at a lower Re relative to the $\overline{u^2}$ and $\overline{v^2}$ stresses, as they are found to be constant across the Re range examined.

Recent high-Re measurements compiled by Marusic *et al.* (2013), suggest that the slope of the logarithmic $\overline{u^2}$ behaviour is universal across pipe (internal) and boundary layer (external) flows. In contrast, a difference in the $\overline{v^2}$ slope has been noted between the internal and external flows ($A_2 \approx 0.5$ in the channel and pipe compared with $A_2 \approx 0.3$ in the boundary layer), albeit at a lower Re (Sillero *et al.* 2013; Chin, Monty & Ooi 2014; Mehrez *et al.* 2019). However, at this Re range, the logarithmic behaviour in $\overline{u^2}$ is also not well defined, and hence the differences in A_2 observed may simply be a low Re effect. Here, we re-examine these differences by decomposing $\overline{v^2}$ based on scales at a matched Re, and the result is presented in figure 10. Close to the wall, the intermediate- (chequered symbols and dash-dotted lines) and large-scale (empty symbols and dashed lines) $\overline{v^2}$ contribution show good agreement between the channel and boundary layer flows, while the differences in the small-scale contributions (solid symbols and dotted lines) are likely due to differences in the spatial resolution between the boundary layer experiments and channel DNS of Lee & Moser (2015).

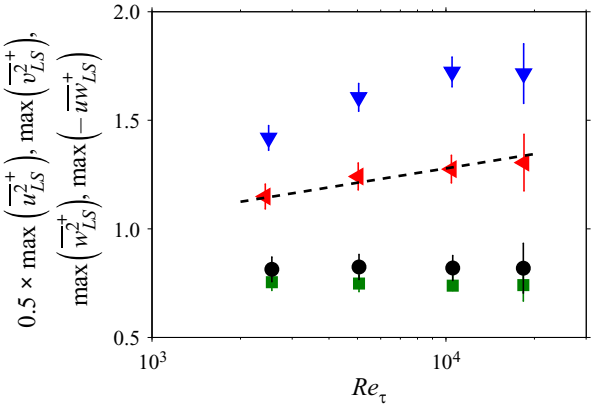

Figure 9. The Re dependency of the maximum large-scale contributions in the turbulent stresses. The turbulent stress contributions are: ▼, $\overline{u^2}$; ◀, $\overline{v^2}$; ■, $\overline{w^2}$; ●, $-\overline{uw}$. Note that the $\overline{u^2}$ contribution is shown premultiplied by a factor 0.5. The dashed line shows a $\log \delta^+$ dependency.

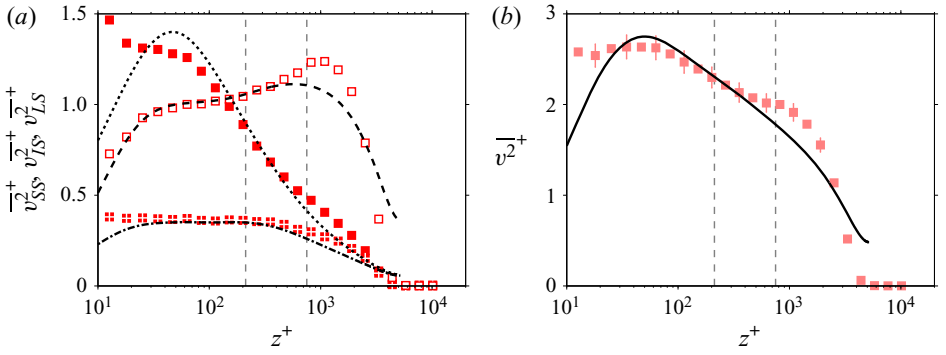

Figure 10. (*a*) Comparison of scale-decomposed $\overline{v^2}$ contributions between the channel (denoted by lines, Lee & Moser 2015) and boundary layer (symbols) flows at $Re_\tau \approx 5000$. The dotted (· · ·), dash-dotted (- · -) and dashed (- - -) lines denote small-, intermediate- and large-scale contributions, respectively, while the symbols are as in figure 8. (*b*) The broadband $\overline{v^2}$ statistics. The vertical dashed lines in panels (*a*,*b*) denote the bounds of the log region.

In the outer region, the maximum difference in $\overline{v^2}$ occurs between the channel and boundary layer flows at $z/\delta \approx 0.33$–0.4, and the differences are most evident at the large scales. In the outer region, the flow is intermittent, i.e. it switches between turbulent and quiescent/non-turbulent states (Chauhan *et al.* 2014; Kwon, Hutchins & Monty 2016). Furthermore, the quiescent core and non-turbulent regions in the channel and boundary layer flows behave differently, which is reflected in the distinct large-scale contributions observed in figure 10(*a*). Thus, although the logarithmic slope exhibited by the broadband $\overline{v^2}$ in the internal and external flows may appear distinct, the results suggest that the $\overline{v^2}$ contributions from the intermediate-scale wall-attached eddies may be universal between these flows. Furthermore, since the wall-attached contributions dominate the broadband $\overline{v^2}$ behaviour at high Re (see § 4.2 for further details), A_2 values in the external and internal flow may exhibit universality at a sufficiently high Re.

4.2. *Revisiting the $\overline{v^2}$ logarithmic behaviour*

Since the sum of $\overline{v^2}_{SS}$, $\overline{v^2}_{IS}$ and $\overline{v^2}_{LS}$ returns the broadband $\overline{v^2}$, their trends in the log region can provide a better insight regarding the behaviour of the cumulative statistic, which follows (3.1) as demonstrated in § 3. Thus, here we fit functional forms to describe the small-, intermediate- and large-scale contributions and suppose that they respectively maintain the viscous, distance-from-the-wall and outer scaling to predict the $\overline{v^2}$ behaviour as a function of *Re*.

Based on an empirical observation from figure 8(*a–c*), log–linear functions are chosen as a first approximation to describe contributions in the log region for all three scales (it will be shown later that the resulting asymptotic prediction holds independently of the $\overline{v^2_{SS}}$ and $\overline{v^2_{LS}}$ functional forms). For the small-scale contributions, the data suggest a $\ln z^+$ dependence (grey solid lines) as indicated in figure 8(*a*). Therefore, the small-scale contributions are modelled as

$$\overline{v^2}^+_{SS} = -C_{S1} \ln z^+ + C_{S2}, \tag{4.3}$$

where C_{S1} and C_{S2} are constants.

Meanwhile, figure 8(*b*) shows increasing $\overline{v^2}^+_{IS}$ contribution with increasing *Re* at a fixed z^+. This is consistent with the eddies responsible for the intermediate-scales following the distance-from-the-wall scaling prescribed by AEH, since the self-similar attached eddy contributions from each hierarchy level are identical. This means that $\overline{v^2}$ at a particular z^+ location is expected to correspond to the number of contributing hierarchy levels, which exhibits a $\log \delta^+$ scaling (Townsend 1976; Perry & Chong 1982). Hence, based on AEH, $\overline{v^2}_{IS}$ is modelled to follow a $\ln (z/\delta)$ dependence. Hence,

$$\overline{v^2}^+_{IS} = f_{I1}(\delta^+) \ln (z/\delta) + f_{I2}(\delta^+), \tag{4.4}$$

where f_{I1} and f_{I2} are functions of the Reynolds number but not of z. Note that the *Re* dependency prescribed for f_{I1} and f_{I2} is based on the logarithm slope and intercept trends observed for the fits (the logarithmic behaviour is hardly present for the $Re_\tau \approx 5000$ case) shown in figure 8(*b*).

The large-scale contributions, $\overline{v^2}_{LS}$, show a collapse as a function of z^+ within the log region, indicating a $\ln z^+$ dependence similar to the small-scale contribution, as demonstrated in figure 8(*c*); therefore,

$$\overline{v^2}^+_{LS} = f_{L1}(\delta^+) \ln z^+ + f_{L2}(\delta^+), \tag{4.5}$$

where f_{L1} and f_{L2} are functions of the Reynolds number but not of z as in (4.4). Here, f_{L1} and f_{L2} are chosen to exhibit an *Re* dependency, since the maximum $\overline{v^2}_{LS}$, shown in figure 9, deviates from a $\log \delta^+$ relation (dashed line) required for an *Re* invariant logarithmic slope and intercept.

Figures 11(*a*) and 11(*d*) show the modelled $\overline{v^2}$ statistics based on the experimental data at $Re_\tau \sim 10^4$. Note that the modelled $\overline{v^2}$ is constructed based on piecewise log–linear functions and follows (4.3)–(4.5) within the log region, demarcated here by the vertical dashed lines. In order to satisfy the distance-from-the-wall scaling for the intermediate-scale, $f_{I1}(\delta^+)$ and $f_{I2}(\delta^+)$ in (4.4) need to approach constants C_{I1} and C_{I2} at sufficiently high *Re* (Townsend 1976). Through an additional assumption that the small- and large-scales remain invariant in the viscous and outer scaling, respectively, the *Re*

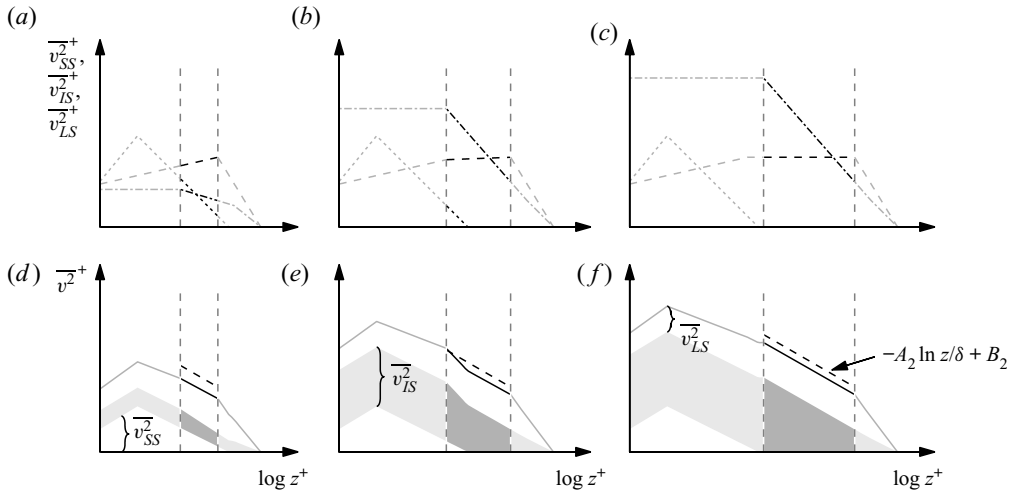

Figure 11. Logarithmic behaviour of $\overline{v^2}$ and its Re dependency. (a,d) $Re_\tau \sim 10^4$ (based on the experimental data), (b,e) $Re_\tau \sim 10^5$ (prediction) and (c,f) $Re_\tau \sim 10^6$ (prediction). (a–c) Scale-decomposed and (d–f) broadband $\overline{v^2}$ statistics. The small- ($\overline{v^2}_{SS}$), intermediate- ($\overline{v^2}_{IS}$) and large-scales ($\overline{v^2}_{LS}$) are denoted by the dotted ($\cdots$), dash-dotted (-$\cdot$-) and dashed (---) lines, respectively, in panels (a–c), while the relative contributions are demarcated by the shaded region in panels (d–f).

dependency of the $\overline{v^2}$ statistics can be predicted, as shown in figure 11 for cases when the scale separation increases by one and two orders of magnitude.

In order to examine the Re dependency of the constants A_2 and B_2 in (3.1), (4.3)–(4.5) is substituted into (4.1) leading to

$$\begin{aligned}\overline{v^2}^+ &= \overbrace{-C_{S1}\ln(z/\delta) - C_{S1}\ln\delta^+ + C_{S2}}^{\overline{v^2_{SS}}} + \overbrace{f_{I1}(\delta^+)\ln(z/\delta) + f_{I2}(\delta^+)}^{\overline{v^2_{IS}}} \\ &\quad + \overbrace{f_{L1}(\delta^+)\ln(z/\delta) + f_{L1}(\delta^+)\ln\delta^+ + f_{L2}(\delta^+)}^{\overline{v^2_{LS}}} \\ &= \underbrace{-\big(C_{S1} - f_{I1}(\delta^+) - f_{L1}(\delta^+)\big)}_{A_2}\ln(z/\delta) \\ &\quad + \underbrace{\big(-C_{S1}\ln\delta^+ + C_{S2} + f_{I2}(\delta^+) + f_{L1}(\delta^+)\ln\delta^+ + f_{L2}(\delta^+)\big)}_{B_2}. \end{aligned} \tag{4.6}$$

Thus, in addition to the term $f_{I1}(\delta^+)$ approaching a constant, Re needs to be sufficiently high such that the small- and large-scale influences in the log region are minimal to observe a universal A_2. The prescribed small-scale invariance in the viscous units means that $\overline{v^2_{SS}}$ remain identical in figure 11(a–c) irrespective of the Re increase. Furthermore, since the start of the log region follows a $\sqrt{\delta^+}$ scaling (Wei *et al.* 2005; Morrill-Winter *et al.* 2017), an increasingly smaller portion of the small-scale fluctuations modelled by (4.3) falls within the log region with increasing Re. Ultimately, the C_{S1} and C_{S2} contributions disappears at $Re_\tau \gtrsim O(10^6)$ (see figure 11c,f). For the $\overline{v^2_{LS}}$ contributions, the log–linear relation in the near-wall and outer regions (the tinted regions) for the $Re_\tau \approx 10^4$ case

is maintained for the high-Re predictions in the viscous and outer units, respectively. Furthermore, $f_{L1}(\delta^+)$ and $f_{L2}(\delta^+)$ in (4.5) are adjusted such that $\overline{v^2_{LS}}$ is continuous at all z locations. Hence, the logarithmic slope, $f_{L1}(\delta^+)$, becomes shallower with increasing Re until it reaches zero and $f_{L2}(\delta^+)$ becomes a constant (see figure 11c). Finally, the $\overline{v^2_{IS}}$ contributions shown in figures 11(a) and 11(c) assumes that $f_{I1}(\delta^+)$ has reached the asymptotic value $-C_{I1}$. Since C_{S1} and $f_{L1}(\delta^+)$ both approach zero in (4.6) at sufficiently high Re, the intermediate-scales are solely responsible for the logarithmic $\overline{v^2}$ behaviour in the asymptotic limit (i.e. $A_2 = C_{I1}$) as demonstrated in figure 11. Note that, although the trends observed for $\overline{v^2}$ may reflect the attached eddy behaviour at very high Re ($Re_\tau \sim O(10^6)$), this does not necessarily hold at a lower Re ($Re_\tau \sim O(10^4)$) where the intermediate-scales are not the dominant contributor to $\overline{v^2}$.

A non-zero C_{S1} leads to a reduced B_2 at a higher Re according to (4.6); however, in reality B_2 is observed to increase with Re (see figure 4). Therefore, the other Re dependent terms, $f_{I2}(\delta^+) + f_{L2}(\delta^+)$, must increase at a rate faster than $O(\ln \delta^+)$. Moreover, based on the intermediate-scales following the distance-from-the-wall scaling, $f_{I2}(\delta^+)$ is expected to asymptote to a constant. Thus, at sufficiently high Re the C_{S1} contribution is expected to disappear while both $f_{I2}(\delta^+)$ and $f_{L2}(\delta^+)$ approach constants, and therefore B_2 becomes a constant.

To summarise the asymptotic behaviour,

$$C_{S1}, C_{S2}, f_{L1}(\delta^+) \to 0 \tag{4.7}$$

and

$$f_{I1}(\delta^+) \to -C_{I1}, \quad f_{I2}(\delta^+) \to C_{I2}, \quad f_{L2}(\delta^+) \to C_{L2}, \tag{4.8a–c}$$

where C_{I1}, C_{I2} and C_{L2} are constants. Consequently, (4.6) simplifies to

$$\overline{v^2}^+ = \underbrace{-C_{I1}}_{-A_2} \ln(z/\delta) + \underbrace{C_{I2} + C_{L2}}_{B_2}, \tag{4.9}$$

in the asymptotic limit. Furthermore, since the only term retained in the asymptotic form from $\overline{v^2_{SS}}$ and $\overline{v^2_{LS}}$ is a constant, C_{L2}, it turns out that (4.9) holds irrespective of the $\overline{v^2_{SS}}$ and $\overline{v^2_{LS}}$ functional forms, provided that $\overline{v^2_{SS}}^+ \to 0$ and $\overline{v^2_{LS}}^+ \to C_{L2}$ as $Re \to \infty$ is satisfied. Note that, if further experiments in the range of $Re_\tau \sim 10^4$–10^6 show a B_2 dependency on Re and do not approach a constant B_2 as predicted by AEH, this can be accommodated in the current model by retaining $f_{I2}(\delta^+)$ and $f_{L2}(\delta^+)$ instead of C_{I2} and C_{L2} in (4.9).

5. Summary and conclusions

The spanwise velocity statistics are examined using a custom subminiature cross-wire probe in high-Reynolds-number turbulent boundary layers. The custom probe is designed to minimise the spatial resolution effects and misalignment errors, based on recommendations from simulated cross-wire studies (Philip *et al.* 2013*b*; Baidya *et al.* 2019*a*,*b*). Furthermore, the current experiments are designed to include cases where a constant spatial resolution is maintained across a range of Reynolds numbers to avoid contamination from the spatial attenuation that can lead to incorrect interpretation of Reynolds number (Re) trends (Hutchins *et al.* 2009).

A logarithmic relation with respect to wall-normal location (z) is observed for the variance of the spanwise velocity, $\overline{v^2}$, in a similar manner to the streamwise velocity

component, u. Although the slope of the logarithmic $\overline{v^2}$ behaviour recorded is slightly dependent on the spatial resolution of the sensors, for matched spatial resolution datasets we find a consistent slope across a range of Re. Hence, the empirical data, in part, supports the AEH of Townsend (1976), in that a constant Re invariant logarithmic slope for $\overline{u^2}$ and $\overline{v^2}$ is predicted. The experimental data indicate that A_2, the slope of logarithmic $\overline{v^2}$ behaviour, is approximately 0.27 based on a linear regression in the log region ($3\sqrt{\delta^+} \leqslant z^+ \leqslant 0.15\delta^+$) at $Re_\tau \approx 10\,000$. It is noted, however, that contrary to Townsend's AEH prediction, the data show a varying value in the intercept of this log law (B_2).

Similar to u, the influence of the large-scale features residing in the log region extends to the wall for the v signal, resulting in a large-scale v footprint in the near-wall region. The dominant energetic scales in v lie between the streamwise (largest) and wall-normal components (smallest), as shown in figure 12. Moreover, unlike for u, energetic contributions from $O(10\delta)$ fluctuations are insignificant in v, and consequently the range of energetic scales is narrower when compared with u. Below $z^+ < 70$, the dominant contribution in the v spectra occurs at scales where the streamwise wavelength is approximately 350 viscous units (i.e. $\lambda_x^+ \approx 350$). In the log region, the peak in the v spectra follows the distance-from-the-wall scaling. Beyond the log region, the dominant contribution in the v spectra again seems to occur at a constant λ_x which is $O(\delta)$. Thus, as shown in figure 6, an energetic ridge is evident in the v-spectrogram, instead of distinct inner and outer energetic sites observed for the u-spectrogram (Hutchins & Marusic 2007*a*). However, similar to the u-spectrogram, the near-wall small-scales are found to be universal in the v-spectrogram (and also in the w-spectrogram and Reynolds shear stress cospectrogram) when scaled in viscous units.

The observed scaling for certain regions in the v-spectrogram can provide insights into the behaviour of the $\overline{v^2}$ statistic by considering it to be a summation of contributions from small-, intermediate- and large-scales. Hence, a modelled $\overline{v^2}$ is constructed from the small-, intermediate and large-scales, which are prescribed to follow the viscous, distance-from-the-wall and outer scaling, respectively. The modelled $\overline{v^2}$ demonstrate that its logarithmic behaviour is not necessarily solely due to attached eddy contributions. Hence, at finite Re, the additional non-attached-eddy contributions may mask the true attached eddy behaviour. As an example, the differences between the $\overline{v^2}$ behaviour in the internal (channel and pipe) and external flows (boundary layer) are found to be a result of differing contributions from the δ-scaled structures. Consequently, the contributions from the attached eddies for the internal and external flow are found to be more similar than their respective $\overline{v^2}$ behaviours would suggest.

Funding. The authors gratefully acknowledge support from the Australian Research Council.

Data repository. The moments and (co)spectra of u, v and w from the current study are available online at https://fluids.eng.unimelb.edu.au/#data.

Declaration of interests. The authors report no conflict of interest.

Author ORCIDs.
R. Baidya https://orcid.org/0000-0002-6148-602X;
I. Marusic https://orcid.org/0000-0003-2700-8435.

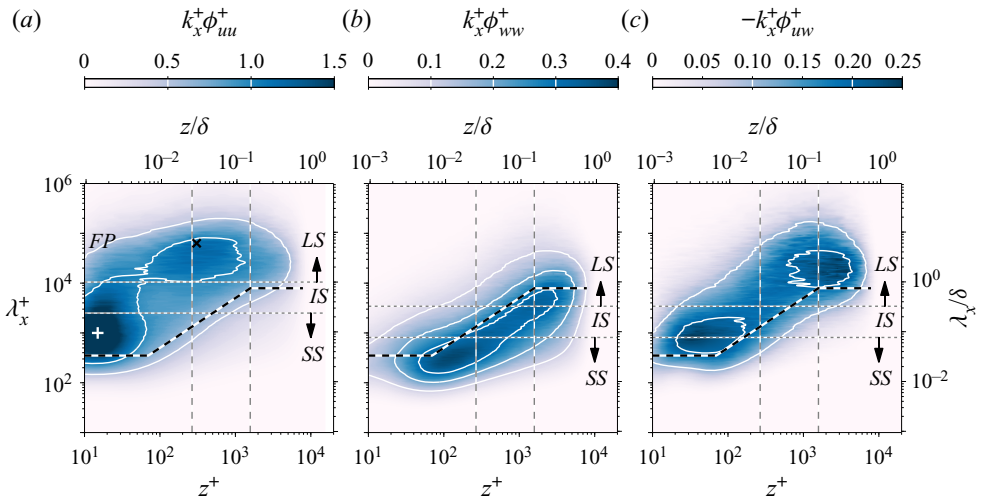

Figure 12. Premultiplied turbulent stress spectrogram as functions of wall height, z, and wavelength, λ_x, at $Re_\tau \approx 10\,000$. (*a*) u-spectrogram, (*b*) w-spectrogram and (c) Reynolds shear stress cospectrogram. The black dashed lines correspond to the location of the energetic ridge shown in figure 6(*c*), while the solid lines indicate contour levels (*a*) 0.5 and 1, (*b*) 0.1, 0.2 and 0.3, (*c*) 0.1 and 0.2, respectively. (*a*) Here '*FP*' denotes the location of the energetic u footprint from the very large-scale structure, while '+' and '×' indicate the location of the inner and outer energetic sites, respectively. The wavelengths corresponding to small-, intermediate- and large-scales are denoted by *SS*, *IS* and *LS*, respectively.

Symbols	x (m)	U_∞ (ms^{-1})	Re_τ	ν/U_τ (μm)	U_τ (ms^{-1})	δ (m)	Δt^+	TU_∞/δ	l_x^+	l_z^+	Δs_y^+
●	2	15.2	2600	28	0.569	0.071	0.513	18 000	14	14	7
■	7	15.2	5100	30	0.526	0.153	0.436	19 000	13	13	7
♦	18	14.8	10 600	32	0.484	0.338	0.377	18 000	12	12	6
▲	18	29.6	18 300	17	0.919	0.308	0.684	20 000	24	24	12

Table 2. Experimental parameters for the cross-wire measurements, configured to measure the streamwise and wall-normal velocities.

Appendix A. Streamwise and wall-normal velocity components

In order to facilitate comparison of v against other components, the equivalent statistics for u, w and the Reynolds shear stress are shown here. The w fluctuations are also obtained using a cross-wire probe with a similar dimension as to that used for measuring v, however, the wires are now arranged to be parallel to the x–z plane and the sensors are now separated by Δs_y in the y direction. The experimental parameters are summarised in table 2, where the $Re_\tau \approx 2500$–$10\,000$ dataset are measurements detailed in Baidya *et al.* (2017). It should be noted that, the u statistics shown in figures 9, 12 and 13 are obtained by combining both cross-wire configurations at nominally matched Re_τ, while the w and Reynold shear stress statistics are solely from the datasets shown in table 2. Moreover, to account for the dominant u energy residing in the larger-scales compared with v, the cutoff wavelengths λ_{c1} and λ_{c2} used to distinguish the small-, intermediate- and large-scale $\overline{u^2}$ contributions are set at

$$\lambda_{c1}^+ = 2500, \quad \lambda_{c2} = \delta. \tag{A1a,b}$$

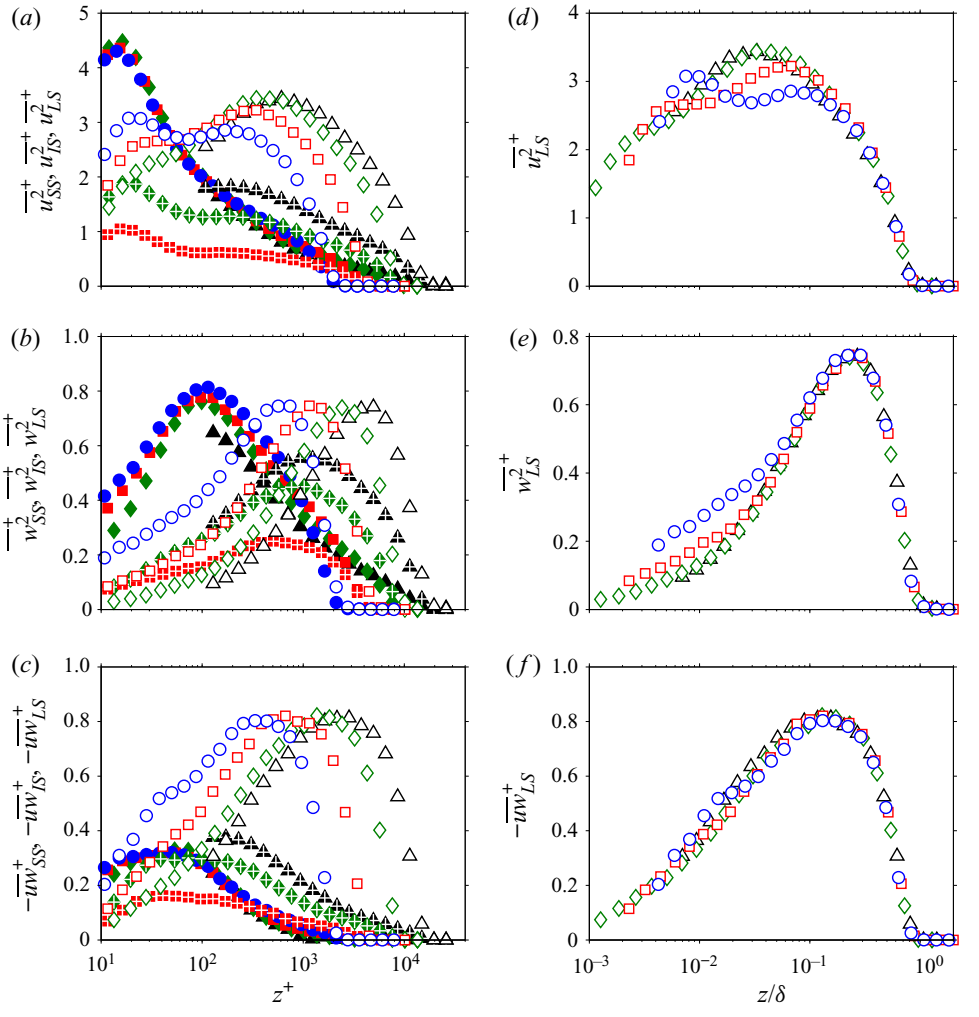

Figure 13. Scale-decomposed $\overline{u^2}$, $\overline{w^2}$ and $\overline{uw}$, shown from top to bottom. (*a–c*) Small-, intermediate- and large-scale contributions as functions of z^+ and (*d–f*) large-scale contributions shown against z/δ. The symbols are as in figure 8.

In contrast, λ_{c1} and λ_{c2} remain unchanged from (4.2) for the $\overline{w^2}$ and Reynolds shear stress statistics. The cutoff wavelengths are indicated by the horizontal dotted lines in figure 12.

References

Abe, H., Kawamura, H. & Choi, H. 2004 Very large-scale structures and their effects on the wall shear-stress fluctuations in a turbulent channel flow up to $Re_\tau = 640$. *J. Fluid Engng* **126** (5), 835–843.

Adrian, R.J., Meinhart, C.D. & Tomkins, C.D. 2000 Vortex organization in the outer region of the turbulent boundary layer. *J. Fluid Mech.* **422**, 1–54.

Baidya, R. 2016 Multi-component velocity measurements in turbulent boundary layers. PhD thesis, University of Melbourne.

Baidya, R., Philip, J., Hutchins, N., Monty, J.P. & Marusic, I. 2019*a* Sensitivity of turbulent stresses in boundary layers to cross-wire probe uncertainties in the geometry and calibration procedure. *Meas. Sci. Technol.* **30**, 085301.

BAIDYA, R., PHILIP, J., HUTCHINS, N., MONTY, J.P. & MARUSIC, I. 2019*b* Spatial averaging effects on the streamwise and wall-normal velocity measurments in a wall-bounded turbulence using a cross-wire probe. *Meas. Sci. Technol.* **30**, 085303.

BAIDYA, R., PHILIP, J., HUTCHINS, N., MONTY, J.P. & MARUSIC, I. 2017 Distance-from-the-wall scaling of turbulent motions in wall-bounded flows. *Phys. Fluids* **29** (2), 020712.

BAIDYA, R., PHILIP, J., MONTY, J.P., HUTCHINS, N. & MARUSIC, I. 2014 Comparisons of turbulence stresses from experiments against the attached eddy hypothesis in boundary layers. In *Proceedings of the 19th Australasian Fluid Mechanics Conference* (ed. H. Chowdhury & F. Alam). RMIT University.

BROWNE, L.W.B., ANTONIA, R.A. & SHAH, D.A. 1988 Selection of wires and wire spacing for ×-wires. *Exp. Fluids* **6** (4), 286–288.

CHAMPAGNE, F.H., SLEICHER, C.A. & WEHRMANN, O.H. 1967 Turbulence measurements with inclined hot-wires. Part 1. Heat transfer experiments with inclined hot-wire. *J. Fluid Mech.* **28** (01), 153–175.

CHAUHAN, K., PHILIP, J., DE SILVA, C.M., HUTCHINS, N. & MARUSIC, I. 2014 The turbulent/non-turbulent interface and entrainment in a boundary layer. *J. Fluid Mech.* **742**, 119–151.

CHAUHAN, K.A., MONKEWITZ, P.A. & NAGIB, H.M. 2009 Criteria for assessing experiments in zero pressure gradient boundary layers. *Fluid Dyn. Res.* **41** (2), 021404.

CHIN, C., MONTY, J.P. & OOI, A. 2014 Reynolds number effects in DNS of pipe flow and comparison with channels and boundary layers. *Intl J. Heat Fluid Flow* **45**, 33–40.

CHOI, H., MOIN, P. & KIM, J. 1994 Active turbulence control for drag reduction in wall-bounded flows. *J. Fluid Mech.* **262**, 75–110.

COLLIS, D.C. & WILLIAMS, M.J. 1959 Two-dimensional convection from heated wires at low Reynolds numbers. *J. Fluid Mech.* **6** (3), 357–384.

DAVIDSON, P.A., NICKELS, T.B. & KROGSTAD, P.-Å. 2006 The logarithmic structure function law in wall-layer turbulence. *J. Fluid Mech.* **550**, 51–60.

DEGRAAFF, D.B. & EATON, J.K. 2000 Reynolds-number scaling of the flat-plate turbulent boundary layer. *J. Fluid Mech.* **422**, 319–346.

DEL ÁLAMO, J.C. & JIMÉNEZ, J. 2009 Estimation of turbulent convection velocities and corrections to Taylor's approximation. *J. Fluid Mech.* **640**, 5–26.

DEL ÁLAMO, J.C., JIMÉNEZ, J., ZANDONADE, P. & MOSER, R.D. 2004 Scaling of the energy spectra of turbulent channels. *J. Fluid Mech.* **500**, 135–144.

FERNHOLZ, H.H. & FINLEY, P.J. 1996 The incompressible zero-pressure-gradient turbulent boundary layer: an assessment of the data. *Prog. Aerosp. Sci.* **32** (4), 245–311.

GATTI, D. & QUADRIO, M. 2016 Reynolds-number dependence of turbulent skin-friction drag reduction induced by spanwise forcing. *J. Fluid Mech.* **802**, 553–582.

HATTON, A.P., JAMES, D.D. & SWIRE, H.W. 1970 Combined forced and natural convection with low-speed air flow over horizontal cylinders. *J. Fluid Mech.* **42** (1), 17–31.

HINZE, J.O. 1975 *Turbulence: an Introduction to its Mechanisms and Theory*. McGraw-Hill.

HULTMARK, M., VALLIKIVI, M., BAILEY, S.C.C. & SMITS, A.J. 2012 Turbulent pipe flow at extreme Reynolds numbers. *Phys. Rev. Lett.* **108** (9), 094501.

HURST, E., YANG, Q. & CHUNG, Y.M. 2014 The effect of Reynolds number on turbulent drag reduction by streamwise travelling waves. *J. Fluid Mech.* **759**, 28–55.

HUTCHINS, N., CHAUHAN, K., MARUSIC, I., MONTY, J. & KLEWICKI, J. 2012 Towards reconciling the large-scale structure of turbulent boundary layers in the atmosphere and laboratory. *Boundary-Layer Meteorol.* **145** (2), 273–306.

HUTCHINS, N. & MARUSIC, I. 2007*a* Evidence of very long meandering features in the logarithmic region of turbulent boundary layers. *J. Fluid Mech.* **579**, 1–28.

HUTCHINS, N. & MARUSIC, I. 2007*b* Large-scale influences in near-wall turbulence. *Phil. Trans. R. Soc. Lond.* A **365**, 647–664.

HUTCHINS, N., NICKELS, T.B., MARUSIC, I. & CHONG, M.S. 2009 Hot-wire spatial resolution issues in wall-bounded turbulence. *J. Fluid Mech.* **635**, 103–136.

HWANG, J. & SUNG, H.J. 2018 Wall-attached structures of velocity fluctuations in a turbulent boundary layer. *J. Fluid Mech.* **856**, 958–983.

JEONG, J., HUSSAIN, F., SCHOPPA, W. & KIM, J. 1997 Coherent structures near the wall in a turbulent channel flow. *J. Fluid Mech.* **332**, 185–214.

JIMÉNEZ, J. & MOIN, P. 1991 The minimal flow unit in near-wall turbulence. *J. Fluid Mech.* **225**, 213–240.

KARNIADAKIS, G.E. & CHOI, K.S. 2003 Mechanisms on transverse motions in turbulent wall flows. *Annu. Rev. Fluid Mech.* **35** (1), 45–62.

KIM, H.T., KLINE, S.J. & REYNOLDS, W.C. 1971 The production of turbulence near a smooth wall in a turbulent boundary layer. *J. Fluid Mech.* **50** (1), 133–160.

KLEWICKI, J.C., SARIC, W.S., MARUSIC, I. & EATON, J.K. 2007 Wall-bounded flows. In *Springer Handbook of Experimental Fluid Mechanics* (ed. C. Tropea, A.L. Yarin & J.F. Foss), vol. 1, chap. 5.2, pp. 229–286. Springer.

KWON, Y.S., HUTCHINS, N. & MONTY, J.P. 2016 On the use of the Reynolds decomposition in the intermittent region of turbulent boundary layers. *J. Fluid Mech.* **794**, 5–16.

LAUFER, J. 1954 The structure of turbulence in fully developed pipe flow. *Tech. Rep.* NACA-TR-1174. National Advisory Committee for Aeronautics.

LEE, M. & MOSER, R.D. 2015 Direct numerical simulation of turbulent channel flow up to $Re_\tau \approx 5200$. *J. Fluid Mech.* **774**, 395–415.

MARUSIC, I., CHAUHAN, K.A., KULANDAIVELU, V. & HUTCHINS, N. 2015 Evolution of zero-pressure-gradient boundary layers from different tripping conditions. *J. Fluid Mech.* **783**, 379–411.

MARUSIC, I. & MONTY, J.P. 2019 Attached eddy model of wall turbulence. *Annu. Rev. Fluid Mech.* **51**, 49–74.

MARUSIC, I., MONTY, J.P., HULTMARK, M. & SMITS, A.J. 2013 On the logarithmic region in wall turbulence. *J. Fluid Mech.* **716**, 716.

MARUSIC, I., UDDIN, A.K.M. & PERRY, A.E. 1997 Similarity law for the streamwise turbulence intensity in zero-pressure-gradient turbulent boundary layers. *Phys. Fluids* **9** (12), 3718–3726.

MATHIS, R., HUTCHINS, N. & MARUSIC, I. 2009 Large-scale amplitude modulation of the small-scale structures in turbulent boundary layers. *J. Fluid Mech.* **628**, 311–337.

MEHREZ, A., PHILIP, J., YAMAMOTO, Y. & TSUJI, Y. 2019 Pressure and spanwise velocity fluctuations in turbulent channel flows: logarithmic behavior of moments and coherent structures. *Phys. Rev. Fluids* **4** (4), 044601.

MENEVEAU, C. & MARUSIC, I. 2013 Generalized logarithmic law for high-order moments in turbulent boundary layers. *J. Fluid Mech.* **719**, R1.

MILLIKAN, C.B. 1938 A critical discussion of turbulent flows in channels and circular tubes. In *Proceedings of the Fifth International Congress for Applied Mechanics* (ed. J.P. den Hartog & H. Peters), pp. 386–392. Wiley.

MONKEWITZ, P.A. & NAGIB, H.M. 2015 Large-Reynolds-number asymptotics of the streamwise normal stress in zero-pressure-gradient turbulent boundary layers. *J. Fluid Mech.* **783**, 474–503.

MONTY, J.P. & CHONG, M.S. 2009 Turbulent channel flow: comparison of streamwise velocity data from experiments and direct numerical simulation. *J. Fluid Mech.* **633**, 461–474.

MORRILL-WINTER, C., KLEWICKI, J., BAIDYA, R. & MARUSIC, I. 2015 Temporally optimized spanwise vorticity sensor measurements in turbulent boundary layers. *Exp. Fluids* **56** (12), 216.

MORRILL-WINTER, C., PHILIP, J. & KLEWICKI, J. 2017 An invariant representation of mean inertia: theoretical basis for a log law in turbulent boundary layers. *J. Fluid Mech.* **813**, 594–617.

NICKELS, T.B. & MARUSIC, I. 2001 On the different contributions of coherent structures to the spectra of a turbulent round jet and a turbulent boundary layer. *J. Fluid Mech.* **448**, 367–385.

NICKELS, T.B., MARUSIC, I., HAFEZ, S. & CHONG, M.S. 2005 Evidence of the k_1^{-1} law in a high-Reynolds-number turbulent boundary layer. *Phys. Rev. Lett.* **95** (7), 074501.

ÖRLÜ, R. & SCHLATTER, P. 2013 Comparison of experiments and simulations for zero pressure gradient turbulent boundary layers at moderate Reynolds numbers. *Exp. Fluids* **54** (6), 1547.

PERRY, A.E. & ABELL, C.J. 1975 Scaling laws for pipe-flow turbulence. *J. Fluid Mech.* **67** (2), 257–271.

PERRY, A.E. & CHONG, M.S. 1982 On the mechanism of wall turbulence. *J. Fluid Mech.* **119**, 173–217.

PERRY, A.E., HENBEST, S. & CHONG, M.S. 1986 A theoretical and experimental study of wall turbulence. *J. Fluid Mech.* **165**, 163–199.

PHILIP, J., HUTCHINS, N., MONTY, J.P. & MARUSIC, I. 2013*a* Spatial averaging of velocity measurements in wall-bounded turbulence: single hot-wires. *Meas. Sci. Technol.* **24** (11), 115301.

PHILIP, J., BAIDYA, R., HUTCHINS, N., MONTY, J.P. & MARUSIC, I. 2013*b* Spatial averaging of streamwise and spanwise velocity measurements in wall-bounded turbulence using $\vee$- and $\times$-probes. *Meas. Sci. Technol.* **24** (11), 115302.

QUADRIO, M. 2011 Drag reduction in turbulent boundary layers by in-plane wall motion. *Phil. Trans. R. Soc. Lond.* A **369** (1940), 1428–1442.

SAMIE, M., MARUSIC, I., HUTCHINS, N., FU, M.K., FAN, Y., HULTMARK, M. & SMITS, A.J. 2018 Fully resolved measurements of turbulent boundary layer flows up to $Re_\tau = 20\,000$. *J. Fluid Mech.* **851**, 391–415.

SCHLATTER, P. & ÖRLÜ, R. 2010 Assessment of direct numerical simulation data of turbulent boundary layers. *J. Fluid Mech.* **659**, 116–126.

SILLERO, J.A., JIMÉNEZ, J. & MOSER, R.D. 2013 One-point statistics for turbulent wall-bounded flows at Reynolds numbers up to $\delta^+ \approx 2000$. *Phys. Fluids* **25** (10), 105102.

SILLERO, J.A., JIMÉNEZ, J. & MOSER, R.D. 2014 Two-point statistics for turbulent boundary layers and channels at Reynolds numbers up to $\delta^+ \approx 2000$. *Phys. Fluids* **26** (10), 105109.

DE SILVA, C.M., WOODCOCK, J.D., HUTCHINS, N. & MARUSIC, I. 2016 Influence of spatial exclusion on the statistical behavior of attached eddies. *Phys. Rev. Fluids* **1** (2), 022401.

SMITS, A.J., MCKEON, B.J. & MARUSIC, I. 2011 High-Reynolds number wall turbulence. *Annu. Rev. Fluid Mech.* **43**, 353–375.

TALLURU, K.M., BAIDYA, R., HUTCHINS, N. & MARUSIC, I. 2014 Amplitude modulation of all three velocity components in turbulent boundary layers. *J. Fluid Mech.* **746**, R1.

TAYLOR, G.I. 1938 The spectrum of turbulence. *Proc. R. Soc. Lond.* A **164** (919), 476–490.

TOWNSEND, A.A. 1976 *The Structure of Turbulent Shear Flow*, 2nd edn. Cambridge University Press.

WEI, T., FIFE, P., KLEWICKI, J. & MCMURTRY, P. 2005 Properties of the mean momentum balance in turbulent boundary layer, pipe and channel flows. *J. Fluid Mech.* **522**, 303–327.

WINTER, K.G. 1979 An outline of the techniques available for the measurement of skin friction in turbulent boundary layers. *Prog. Aerosp. Sci.* **18**, 1–57.

WOODCOCK, J.D. & MARUSIC, I. 2015 The statistical behaviour of attached eddies. *Phys. Fluids* **27** (1), 015104.

YANG, X.I.A., BAIDYA, R., LV, Y. & MARUSIC, I. 2018 A hierarchical random additive model for the spanwise and wall-normal velocities in wall-bounded flows at high Reynolds numbers. *Phys. Rev. Fluids* **3** (12), 124606.

ZIMMERMAN, S., MORRILL-WINTER, C. & KLEWICKI, J. 2017 Design and implementation of a hot-wire probe for simultaneous velocity and vorticity vector measurements in boundary layers. *Exp. Fluids* **58** (10), 148.

ZIMMERMAN, S., *et al.* 2019 A comparative study of the velocity and vorticity structure in pipes and boundary layers at friction Reynolds numbers up to 10^4. *J. Fluid Mech.* **869**, 182–213.